ELSEVIER

Journal of Nuclear Materials 229 (1996) 57–64

journal of nuclear materials

1.4. Mechanical behavior

Measurement and prediction of texture development during a rolling sequence of Zircaloy-4 tubes

R.A. Lebensohn [a], M.I. González [b], C.N. Tomé [a,1], A.A. Pochettino [b]

[a] *Instituto de Física Rosario (CONICET-UNR), 27 de Febrero 210 Bis., 2000 Rosario, Argentina*
[b] *Gerencia de Desarrollo, CNEA, Av. Libertador 8250, 1429 Buenos Aires, Argentina*

Received 19 October 1994; accepted 4 May 1995

Abstract

In this work we compare measurements and numerical predictions of texture development along a forming sequence of Zircaloy-4 tubes. Simulations were carried out using a viscoplastic self-consistent (VPSC) formulation in order to account for the effect of the high intrinsic plastic anisotropy of hcp crystals. Using a set of active slip and twinning systems with associated critical resolved shear stresses – selected in agreement with previously reported experimental evidence – we were able to reproduce the main features of the rolling textures along the complete sequence. Finally, we discuss the effect of different initial parameters (Q-factor, the area-reduction factor, initial texture) on the final texture of the tube.

1. Introduction

Zirconium alloys are widely used in the nuclear industry for different applications. Due to the hcp structure of low alloyed Zirconium, single crystals are usually highly anisotropic and, as a consequence, the in-reactor performance of Zr-alloy polycrystal reactor components and their relevant properties (such as thermal expansion, irradiation creep and growth, hydride orientation, etc.), are strongly affected by the final texture of the specimen.

In this work, we are concerned with the manufacturing process of Zircaloy-4 cladding tubes, which are used in various types of reactors. Starting from an intermediate product: an extruded, reduced and recrystallized (TREX [2]) tube, this process consists of a sequence of rolling passes. After each pass, tube is heat-treated at a certain annealing temperature, which is sufficient to induce recrystallization, except for the last heat treatment which is done just for stress relieving. Both rolling and recrystallization processes have associated texture changes. Therefore, the final texture of the cladding tube depends on the subsequent mechanical and thermal treatments. This final texture must fulfill certain conditions, i.e.: a high radial texture factor (F_r) improves the fracture ductility of the cladding tube.

During each rolling step, three relevant features affect the texture evolution of a tube: (a) the initial texture, (b) the area reduction and the applied strain path. While the former is determined by the previous thermomechanical treatments, the latter depends on the characteristics and configuration of the rolling tools.

The area-reduction factor (R_a) for each rolling step are defined as

$$R_a = \frac{A - a}{A} \times 100, \tag{1}$$

where A and a are cross-sectional area of the tube before and after the rolling step.

Different applied strain path determine different relative changes in the diameter and wall thickness of the tube. The relationship between the relative varia-

[1] Permanent Address: AECL Research, Whiteshell Laboratories, Manitoba, Canada ROE 1LO.

[2] Acronym for tube reduced extrusion.

SSDI 0022-3115(95)00210-3

tions of the wall thickness and the tube external diameter is known as strain-ratio factor or Q-factor.

$$Q = \frac{(E-e)/E}{(D-d)/D}, \tag{2}$$

where E, D and e, d are the thickness and the external diameter before and after the rolling step, respectively.

Different area-reduction and Q-factors [1] give different deformation textures after a given rolling step. Thus, changes in these factors along the manufacturing process can lead to different textures of the final product. However, the complete set of area-reduction factors and Q-factors cannot be arbitrarily chosen since the rolling sequence must fulfill precise requirements for the final dimensions of the tube.

Complex polycrystal models for numerical prediction of deformation processes have undergone an important development during the last years. In this work we show how these models can be used in relation with technological requirements from the nuclear industry, to obtain well-defined final textures for cladding tubes. Realistic simulations of deformation texture development of anisotropic materials, such as Zr alloys, can be done using the viscoplastic self-consistent model (VPSC) [2]. The VPSC model, used in combination with a volume fraction transfer scheme (VFT) [3] to deal with twinning reorientation, has been recently applied to calculations of texture development of Zr alloys at different temperatures and under different strain states [2,4,5].

After describing the experimental and modelling details in Section 2 and 3, respectively, we will compare rolling textures at different stages of the manufacturing process and the corresponding predictions, calculated with the VPSC + VFT model (Section 4). In this way, we will show the influence of the initial texture and the area-reduction and Q-factors on the final texture and, moreover, we will be able to characterize the deformation mechanisms acting at microscopic level during the rolling process. Finally, in Section 5, we will link the evolution of the radial texture factor of the tube with the initial texture and the applied strain, and identify the more efficient Q-factors in relation with the desired final properties of the tube.

2. Experimental

Crystallographic textures were measured by X-ray diffraction after each rolling step and each heat treatment for a rolling sequence of Zircaloy-4 cladding tubes. The manufacturing route, starting from a TREX tube, is schematically represented in Fig. 1. Labels L1 to L4 correspond to as-rolled samples, while labels L1R to L4R are assigned to as-annealed samples. The Q and the area-reduction factors for each pass in the rolling sequence are reported in Table 1.

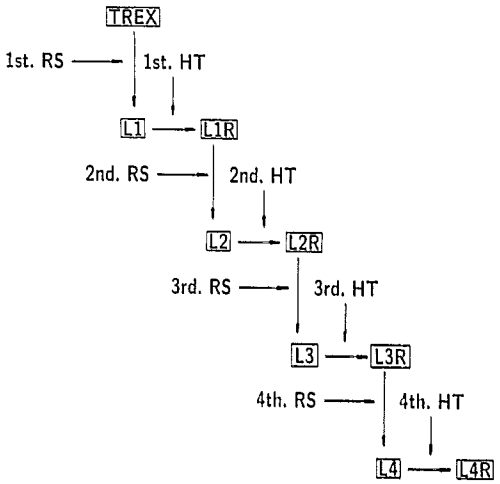

Fig. 1. Schematic representation of a 4-passes rolling sequences of Zircaloy-4 tubes (RS: rolling step, HT: heat treatment).

Complete (0002) and (10$\bar{1}$0) pole figures were obtained by X-ray diffraction, using Cu Kα radiation. The reflection-transmission technique was employed for the determination of the complete pole figures. The reflection method was used for samples inclinations between 0 and 70° while the transmission method was used between 60 and 90°. The intensities in the overlapping region were treated using Pernot's method [6]. Background corrections, defocalization corrections for reflection measurements and absorption corrections for transmission measurements were applied to diffracted intensities.

Table 1
Q-factor, area reduction factor (R_a), Von Mises equivalent strain (ε_{eq}) and applied strain-rate ($\dot{E}$) for each step in the rolling sequence of Zircaloy-4 tubes

Step	Q	R_a	ε_{eq}	$\dot{E}$		
L1	1.8	70%	1.25	1.0	0.0	0.0
				0.0	−0.33	0.0
				0.0	0.0	−0.67
L2	1.7	68%	1.07	1.0	0.0	0.0
				0.0	−0.28	0.0
				0.0	0.0	−0.72
L3	1.5	65%	1.02	1.0	0.0	0.0
				0.0	−0.36	0.0
				0.0	0.0	−0.64
L4	5.5	53%	0.75	1.0	0.0	0.0
				0.0	−0.11	0.0
				0.0	0.0	−0.89

Samples were prepared as follows: (1) machining of the exterior and interior tube walls up to 0.2 mm width; (2) thinning by chemical attack up to 0.05 mm for reflection samples and 0.01 mm for transmission samples; (3) elastic bending, to obtain a flat surface.

3. Modelling

Zr alloys exhibit high plastic anisotropy and non-negligible twinning activity at low temperature. Therefore, a model for texture development calculation of these kind of materials must take into account the strong directionality of the single crystal properties and the effect of twinning reorientation. A code based on the VPSC formulation and the VFT scheme has shown to be a suitable numerical tool for these purposes. Within the VPSC model each grain is regarded as a viscoplastic inclusion deforming inside a fully anisotropic homogeneous equivalent medium (HEM) whose properties are found as an average over the whole polycrystal (v.g.: the VPSC is a *one-site approach*). On the other hand, VFT is an Eulerian scheme that allows to keep track of the exact twinned volume fractions by using invariant orientations during the calculation and updating the associated volume fractions. The VPSC + VFT model accounts for grain reorientation takes place through crystallographic slip, twinning activity, and grain shape effects coupled with the non-homogeneous character of the deformation. Complete descriptions of VPSC and VFT can be found in Refs. [2] and [3], respectively.

Essentially, a texture development calculation consists of successive plastic strain increments imposed to a polycrystal having a given initial texture. In what follows, the experimental textures measured after each heat treatment are used as input for the simulation of the subsequent rolling step (i.e.: TREX is taken as input texture for the simulation of pass L1, L1R for L2, etc.). In fact processing the original experimental data, we built a set of orientations with associated weight factors. For this discrete set of orientations, the radial texture factor can be calculated as

$$F_r = \sum_g \cos^2 \theta_g^r \times \omega_g, \tag{3}$$

where g runs over the complete set of grains, w_g is the weight factor associated with grain g ($\Sigma_g w_g = 1$) and θ_g^r is the angle between the direction of the basal pole of grain g and the radial direction of the tube. Similar expressions can be written for the tangential and the axial texture factors.

Imposing a macroscopic (homogeneous) strain-rate $\dot{E}$, the plastic response and the corresponding grain reorientation are calculated along a given time step Δt in such a way that the resulting Von Mises equivalent strain after that time step is about 0.01. Successive time steps are imposed until the final equivalent strain is reached.

In the most general case of tube rolling the imposed $\dot{E}$ adopts the form

$$\dot{E} = \begin{bmatrix} 1 & 0 & 0 \\ 0 & -\dot{\epsilon}_2 & 0 \\ 0 & 0 & -\dot{\epsilon}_3 \end{bmatrix}, \tag{4}$$

where the tube axis parallel to x_1, the hoop direction is parallel to x_2 and the tube radius is along x_3. In Eq. (1) is $0 \leq \dot{\epsilon}_2,\ \dot{\epsilon}_3 \leq 1$, and since $\dot{E}$ must be traceless, then $(\dot{\epsilon}_2 + \dot{\epsilon}_3) = 1$. The applied strain-rate, together with the Von Mises equivalent strain (ϵ_{eq}) are shown in Table 1 for each rolling pass in the tube forming sequence.

Within the VPSC formulation, the description of the local plastic behavior (i.e., at grain level) depends on the selection of the active deformation modes and their associated critical resolved shear stresses (CRSS). This selection, for the case cold-rolled Zr alloys, has been widely discussed in previous works [2–4]. As a matter of fact, this selection is not unique: it depends on the alloying, the microstructure and the accumulated strain, among other factors. The experimental evidence shows that $\{10\bar{1}0\}\langle 1\bar{2}10\rangle$ *prismatic* $\langle a\rangle$ *slip* (*pr*$\langle a\rangle$) is the softest and, therefore, the most active deformation mode [7–10]. However, the accommodation of strain along the crystallographic $\langle c\rangle$-axis requires the activation of harder modes such as $\{10\bar{1}2\}\langle\bar{1}011\rangle$ *tensile twinning (ttw)* [7–10], $\{2\bar{1}\bar{1}2\}\langle 2\bar{1}\bar{1}3\rangle$ *compressive twinning (ctw)* [7–10] or $\{10\bar{1}1\}\langle 11\bar{2}3\rangle$ *pyramidal* $\langle c+a\rangle$ *slip* (*pyr*$\langle c+a\rangle$) [11,12].

Lebensohn and Tomé [4] have shown that a good qualitatively agreement with the experimental textures and deformations systems activity [7–15] for cold-rolled Zr alloys can be obtained selecting pr$\langle a\rangle$, ttw, and either ctw or pyr$\langle c+a\rangle$ as active deformation modes, with their relative CRSSs satisfying the relation $\tau_{\mathrm{pr}\langle a\rangle} < \tau_{\mathrm{ttw}} < \tau_{\mathrm{ctw}}$ or $\tau_{\mathrm{pyr}\langle c+a\rangle}$. We will show that in the case of the aforementioned tubing sequence, there is a good agreement with several aspects of the measured textures and the VPSC simulations carried out with $\tau_{\mathrm{pr}\langle a\rangle} = 1.0$, $\tau_{\mathrm{ttw}} = 1.5$ and $\tau_{\mathrm{pyr}\langle c+a\rangle} = 4.0$ (arbitrary units). Moreover, since a homotetic hardening law is assumed, the relative critical stresses are not changed during the calculation.

4. Results

In what follows, we present the comparison between measured and calculated (0002) and $\{10\bar{1}0\}$ poles figures (PF) for each of the rolling steps listed in Table 1. At the top of each figure, we display the PF mea-

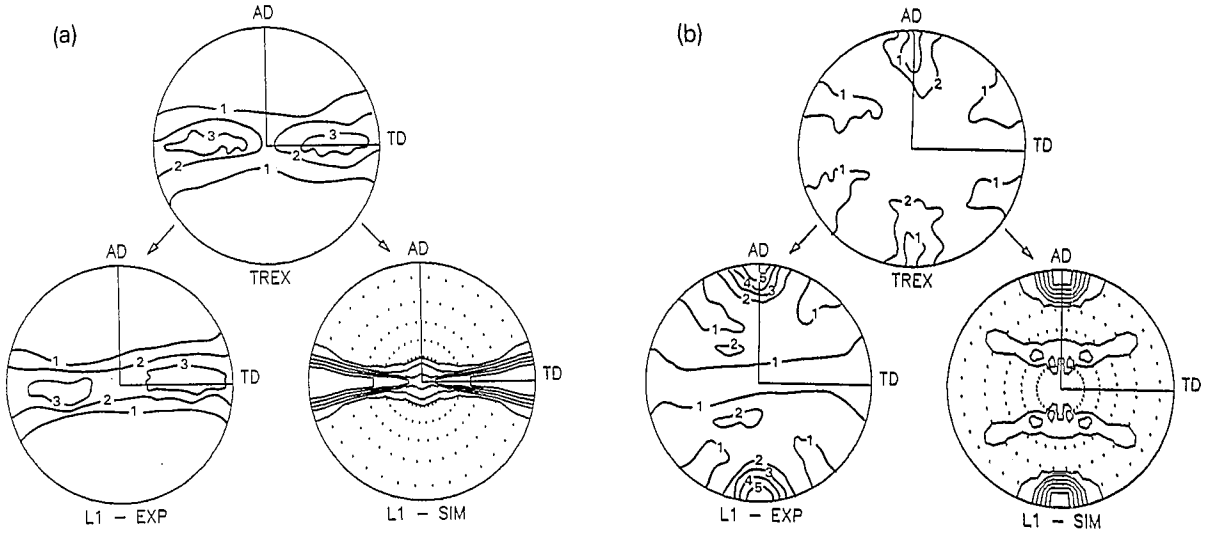

Fig. 2. Experimental (EXP) and simulated (SIM) textures after the first rolling step (from TREX to L1). Lines are multiples of random distribution (mrd). Dots indicate intensity lower than 1 mrd. (a) (0002) and (b) $\{10\bar{1}0\}$ poles figures.

sured after each heat treatment, v.g.: TREX, L1R, L2R and L3R. These annealing textures are used as initial input texture for the simulation of each rolling pass. At the bottom, we show the PFs of both experimental (labeled EXP) and simulated (labeled SIM) rolling textures. Lines represent multiple of random distribution (mrd) and dots are plotted for regions where the calculated intensity remains below 1 mrd.

Fig. 2 shows the basal and prismatic PFs corresponding to the first rolling step. The initial TREX texture has a basal maximum in radial direction (RD)–tangential direction (TD) plane, tilted 55° from RD to TD while prismatic poles show a large spread, being close to an uniform distribution. After rolling with a low Q-factor, the measured basal PF (Fig. 2a) remains almost unchanged while the predicted texture shows a reinforcement in the main texture component, which is not present in the measured L1 texture. Concerning prismatic poles after L1 rolling step (Fig. 2b), a good agreement between measured and predicted PFs is observed. During the rolling process, prismatic poles are reorientated towards the axial direction (AD).

Both effects described earlier, can be explained in terms of a high pr$\langle a \rangle$ slip activity. Table 2 shows the relative activity of the deformation modes corresponding to the simulation of rolling step L1. Evidently, pr$\langle a \rangle$ is the dominant mode throughout the calculation. This high pr$\langle a \rangle$ activity implies a low (but not null) reorientation rate of basal poles. In fact, when a grain deforms by pr$\langle a \rangle$ slip, the $\langle c \rangle$-axis reorientation takes place only due to a local rotation associated with the evolution of the grain shape and the non-uniform character of the deformation [2]. On the other hand, pr$\langle a \rangle$ slip implies a high reorientation rate of prismatic poles provided crystal rotation due to pr$\langle a \rangle$ slip are just simple rotations around the crystallographic $\langle c \rangle$-axis.

Fig. 3 shows PFs corresponding to the second rolling step L2, starting from the recrystallized sample L1R. Differences between L1 and L1R textures, can be ascribed to recrystallization effects, namely: (1) the basal maximum in RD–TD plane rotates about 20° towards RD, (2) the hexagonal prism rotates about 30° around its $\langle c \rangle$ axis and, consequently, the prismatic maximum moves out from AD. Same textures changes due to recrystallization have been reported by Tenckhoff and Rittenhouse in Zircaloy-2 tubes [16]. Unlike the first rolling step, substantial changes in basal PF appear after the pass L2. Basal maxima are formed in RD–TD plane, tilted about 30° from RD but also in RD-AD plane, at 15° from RD. The latter maximum in RD–AD plane has also been reported by other authors [17]. Both maxima are present in the calculated texture but the predicted tilt angle from RD towards AD of the maximum in the RD–AD plane is higher than the actual one. Since the Q-factor for L2 is not very different from the one for L1, it is evident that the difference between both final textures are due to dif-

Table 2
Calculated relative activity of deformation modes for rolling step L1

ε^{eq}	Relative activity		
	pr$\langle a \rangle$	ttw	pyr$\langle c+a \rangle$
0.01	93.7%	6.3%	0.0%
0.63	99.6%	0.4%	0.0%
1.25	96.7%	0.2%	3.1%

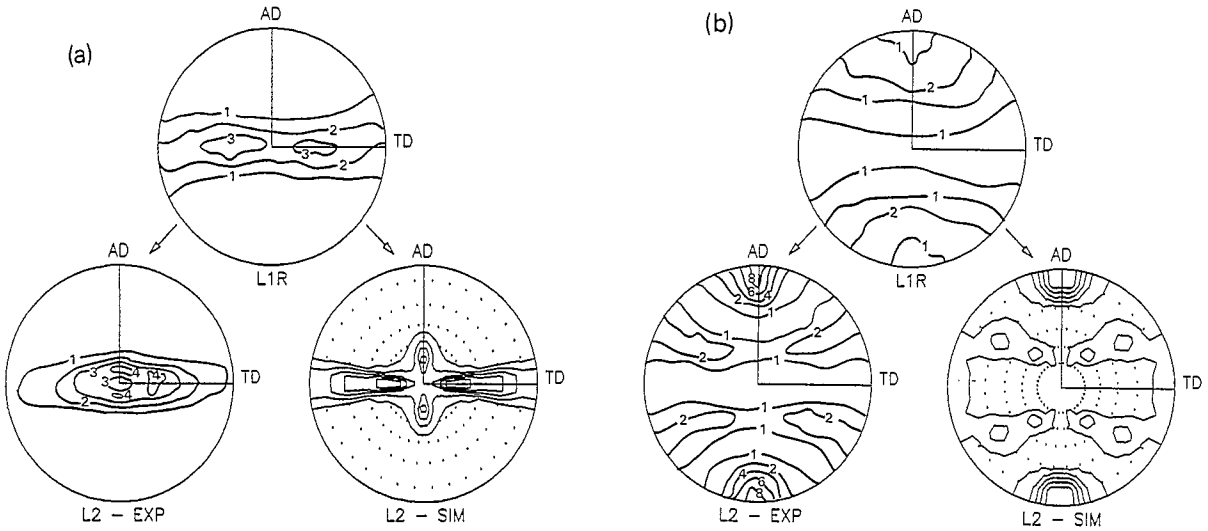

Fig. 3. Experimental (EXP) and simulated (SIM) textures after the second rolling step (from L1R to L2). Lines are multiples of random distribution (mrd). Dots indicate intensity lower than 1 mrd. (a) (0002) and (b) $\{10\bar{1}0\}$ poles figures.

ferences in the respective initial textures. The fact that the L1R tube has a radial texture factor higher than the TREX tube induces a higher activity of the secondary pyr$\langle c+a\rangle$, specially during the second half of the rolling process (see Table 3), leading to a higher reorientation rate of basal poles. Finally, prismatic PF's after this second rolling step (Fig. 3b) are very similar to the ones corresponding to L1: a high concentration in AD due to a still dominant pr$\langle a\rangle$ slip.

Table 3
Calculated relative activity of deformation modes for rolling step L2

ε^{eq}	Relative activity		
	pr$\langle a\rangle$	ttw	pyr$\langle c+a\rangle$
0.01	93.3%	6.7%	0.0%
0.53	99.5%	0.5%	0.0%
1.07	85.9%	4.7%	9.4%

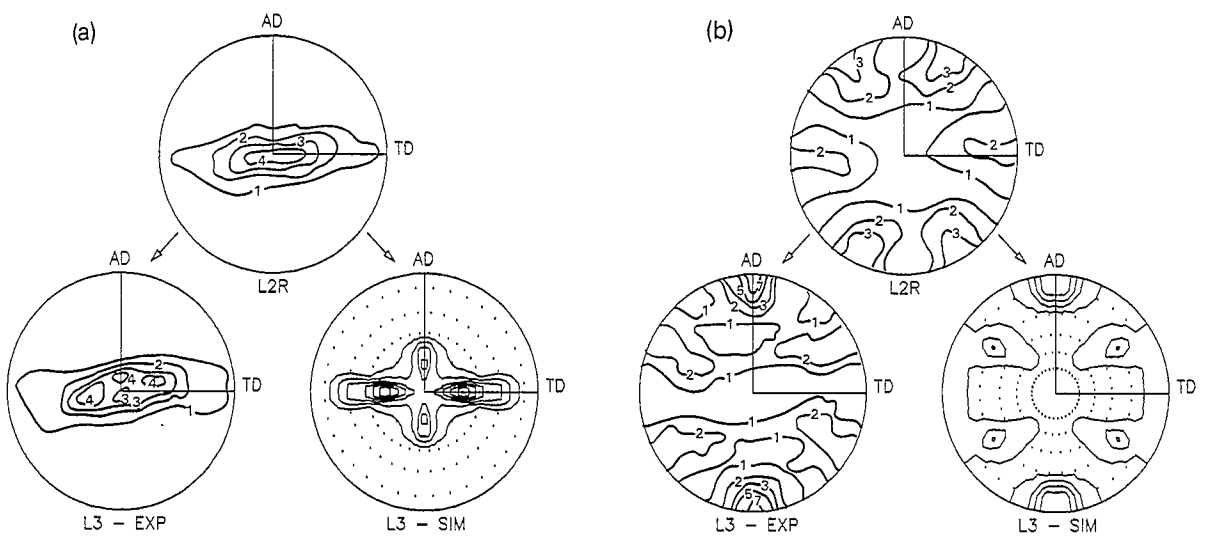

Fig. 4. Experimental (EXP) and simulated (SIM) textures after the third rolling step (from L2R to L3). Lines are multiples of random distribution (mrd). Dots indicate intensity lower than 1 mrd. (a) (0002) and (b) $\{10\bar{1}0\}$ poles figures.

Table 4
Calculated relative activity of deformation modes for rolling step L3

ε^{eq}	Relative activity		
	pr$\langle a \rangle$	ttw	pyr$\langle c+a \rangle$
0.01	93.9%	6.1%	0.0%
0.51	97.7%	0.7%	1.6%
1.02	78.8%	1.4%	19.8%

Table 5
Calculated relative activity of deformation modes for rolling step L4

ε^{eq}	Relative activity		
	pr$\langle a \rangle$	ttw	pyr$\langle c+a \rangle$
0.01	91.9%	8.0%	0.1%
0.37	74.0%	2.9%	23.1%
0.75	70.6%	2.7%	26.7%

Fig. 4 shows the results for the third rolling step: from L2R to L3. The recrystallized tube L2R exhibits a basal maximum in RD. The formation of this maximum can be explained in terms of the reorientation towards RD of the RD–TD and RD–AD maxima appearing in the previous as-rolled tube L2. Texture evolution during this third rolling step is very similar to that corresponding to the former L2 step, namely: two basal maxima in RD–TD, together with a prismatic maximum in AD, appear after rolling. Once again, those maxima are predicted by the VPSC model but the tilt angle of the RD–AD maximum is higher than the measured one. Moreover, the intensity of the basal maximum in the RD–TD is higher in the predicted than in the measured texture. The relative activities for steps L2 and L3 (Table 4) are also similar but in the latter case, a well-defined inial radial texture is responsible of an even higher activity of pyr$\langle c+a \rangle$ slip.

Unlike the former cases, the last rolling step – from L3R to L4, Fig. 5 – is characterized by a high Q-factor. On the other hand, the initial texture L3R is similar to L2R for the same aforementioned reasons: Basal maxima in L3 are tilted towards RD during the recrystallization process. Therefore, differences between L3 and L4 textures are mainly due to different applied strain paths. The actual L4 basal PF (Fig. 5a) is almost axisymmetric with respect to RD: the maximum is distributed along a 'fiber' that surrounds the RD and that cuts the RD–TD plane at 30° and the RD–AD plane at 15° from RD. This effect is only partially reproduced by the calculations. The theoretical results show well-defined maxima appearing in RD–TD and RD–AD planes while the predicted intensity inside the 'fiber' is appreciably lower outside these planes. The effect of a high Q-factor on prismatic poles can be seen in Fig. 5b. The intensity of the prismatic maximum in AD is lower than the intensity for the former rolling steps and a good agreement between experimental and predicted PFs is obtained. The relative activity table (Table 5) shows that pyr$\langle c+a \rangle$ activity is the highest among the four rolling steps considered here.

5. Discussion

We have found an acceptable agreement between several aspects of the actual sequence of rolling textures and the corresponding predictions. The VPSC modelling has proven to be suitable to predict – at least, qualitatively – the effect of the different input

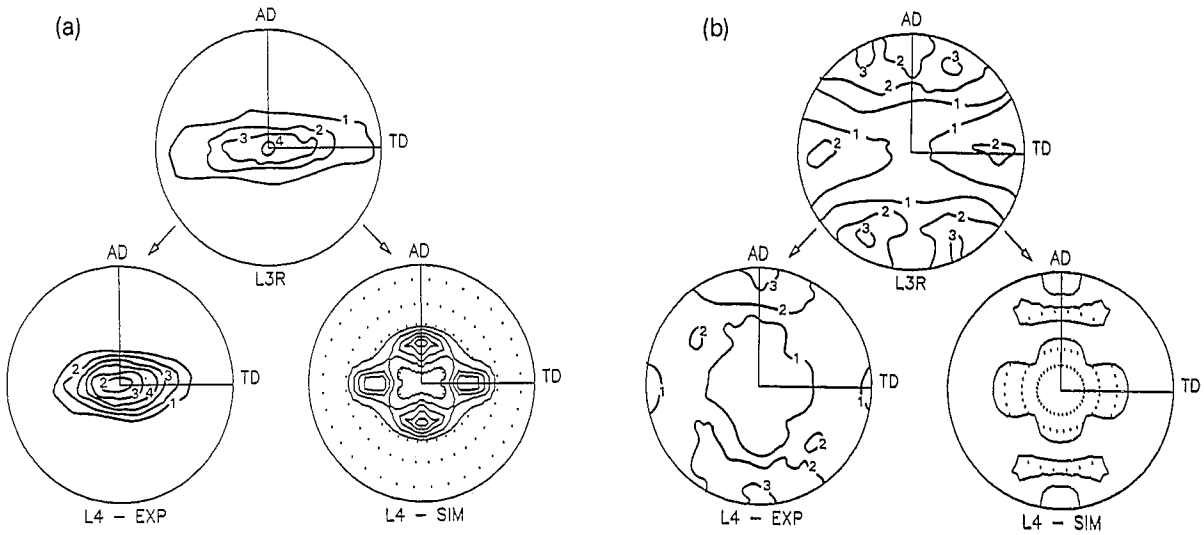

Fig. 5. Experimental (EXP) and simulated (SIM) textures after the fourth rolling step (from L3R to L4). Lines are multiples of random distribution (mrd). Dots indicate intensity lower than 1 mrd. (a) (0002) and (b) $\{10\bar{1}0\}$ poles figures.

parameters (v.g.: initial texture, area reduction, applied strain-path) on the final texture of the rolled tube.

We have also found some discrepancies between the measured and the predicted textures. This difference may be due to some intrinsic limitations of our modelling, i.e., the assumptions of homogeneous macroscopic strain or non correlation between the plastic behavior of a twin and its parent grain. Macroscopic heterogeneities can be taken into account performing a finite elements calculation. In this case, the VPSC could be used for describing the plastic behavior and the texture development of each element. On the other hand, the actual correlation between the plastic behavior of a twin and the parent grain can be taken into account switching from the present one-site model to a two-site approach [18].

Concerning the active deformation modes, their associated CRSSs, and their relative activities, we are aware that they most probably vary during the forming process. Nevertheless, the reasonable agreement with the experimental evidence seems to indicate that the values used here are qualitatively correct. It is worth noting at this point the flexibility of the VPSC scheme, which permits to accommodate most of the deformation in the grains by means of the easier prism slip.

Modelling deformation processes of materials can be used to improve the final product performance. Specifically, the prediction of texture development is useful for the design of new manufacturing routes. An appropriate use of them can diminish the number of expensive in-plant experiments. Fig. 6 displays the dependence of the final radial texture factor with the initial radial texture factor after a single rolling pass

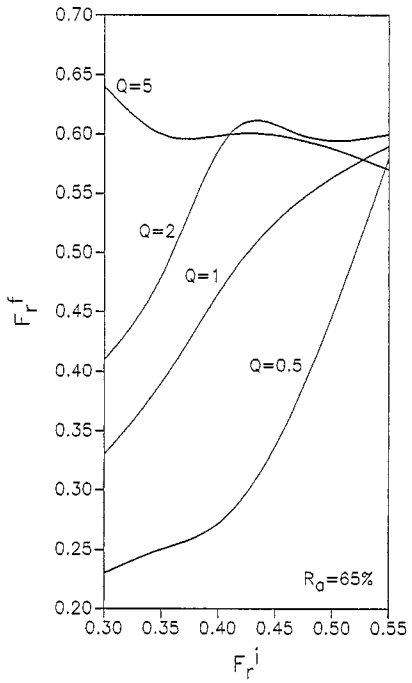

Fig. 6. Predicted final radial texture factor (F_r^f) as a function of the initial radial texture factor (F_r^i) for different values of the Q-factor and a for given area-reduction factor ($R_a = 65\%$).

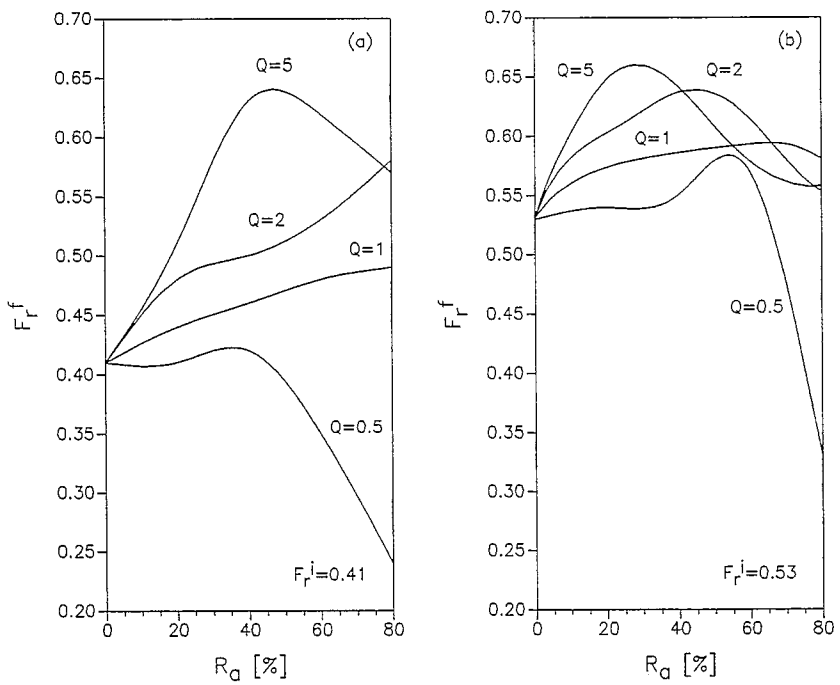

Fig. 7. Predicted final radial texture factor (F_r^f) as a function of the area-reduction factor (R_a) for different values of the Q-factor and for a given initial radial texture factor.

for a fixed area-reduction factor ($R_a = 65\%$). The calculations were done for different Q-factors using the VPSC model and the same set of deformation modes and CRSSs described in Section 4. Several initial textures were considered, having their basal maximum in RD–TD plane at different tilt angles from RD towards TD (hence, for lower tilt angles, higher radial textures factors). Regarding the curves, we can conclude that: (1) For Q-factors equal or higher than 1, the predicted final F_r is always higher than the initial F_r, irrespective of the initial texture or the applied strain path, which indicates a tendency of the $\langle c \rangle$-axis to align with the compressive direction. (2) On the other hand, for a Q-factor lower than 1 the predicted F_r decreases after the rolling pass, except for the case of having a high initial F_r (> 0.50). (3) Rolling with high Q-factor gives higher final F_r when the initial F_r is lower than 0.40 approximately. (4) When the initial F_r is higher than 0.40 and for this area-reduction factor, the final F_r is only marginally larger independently of Q-factor imposed, and there is not a clear relation between the Q-factor and the final F_r.

Finally, Fig. 7 displays the predicted final radial texture factor as a function of the area reduction factor for different Q-factors. Two fixed initial textures having different F_rs (i.e., $F_r^i = 0.41$ and $F_r^i = 0.53$) are adopted as input textures. Curves in Fig. 7a show that for different area-reduction factors, higher values of the Q-factor make for the obtainment of higher final F_rs, although the difference between cases $Q = 2$ and $Q = 5$ are less evident for large values of area-reduction factor. Moreover, it is worth noting that for $Q = 0.5$ very low F_r values are obtained when rolling up to a high area-reduction factor. In the case of a higher initial F_r (Fig. 7b) it is interesting to analyze the appearance of a relative maximum in each curve for Q-factors equal or higher than 1. For increasing values of Q-factors, this maximum occurs at smaller values of area-reduction factor, while its height increases. This theoretical result seems to indicate that a final rolling pass with a high Q-factor and a relatively low area-reduction factor can provide a high radial texture factor, in order to improve the fracture ductility of the cladding tube.

Acknowledgements

This work was partially supported by the Proyecto Multinacional de Materiales (OEA-CNEA).

References

[1] K. Kallstrom, Can. Metall. Quart. 11 (1972) 1985.
[2] R.A. Lebensohn and C.N. Tomé, Acta Metall. Mater. 41 (1993) 2611.
[3] C.N. Tomé, R.A. Lebensohn and U.F. Knocks, Acta Metall. Mater. 39 (1991) 2667.
[4] R.A. Lebensohn and C.N. Tomé, Mater. Sci. Eng. A 175 (1994) 71.
[5] R.A. Lebensohn, P.V. Sanchez and A.A. Pochettino, Scripta Metall. Mater. 30 (1994) 481.
[6] M. Pernot, thèse d'Etat, Université Paris XI, Orsay, France (1977).
[7] E.J. Rapperport, Acta. Metall. 7 (1959) 354.
[8] R.E. Hill, in: Deformation Twinning, eds. R.E. Hill, J.P. Hirth and H.C. Rogers, Metall. Soc. Conf. 25 (1964) 295.
[9] E. Tenckhoff, in: Zirconium in Nuclear Applications, ASTM-STP 551 (American Society for Testing and Materials, Philadelphia, 1982) p. 179.
[10] E. Tenckhoff, Metall. Trans. 9A (1978) 1401.
[11] E. Tenckhoff, Z. Metallkd. 63 (1972) 192.
[12] A. Pochettino, N. Gannio, C. Vial-Edwards and R. Penelle, Scripta Metall. Mater. 27 (1992) 1959.
[13] E. Tenckhoff, in: Proc. 5th Int. Symp. on Zirconium in the Nuclear Industry, ASTM-STP 754, ed. G. Franklin (American Society for the Testing and Materials, Philadelphia, 1982) p. 5.
[14] D. Charquet, E. Alheritiere and G. Blanc, in: Proc 7th Int. Symp. on Zirconium in Nuclear Industry, ASTM-STP 939, eds. R.B. Adamson and L.F.P. Van Swam (American Society for Testing and Materials, Philadelphia, 1987) p. 663.
[15] M.J. Philippe, C. Esling and B. Hocheid, Textures Microstructures 7 (1988) 265.
[16] E. Tenckhoff and P.L. Rittenhouse, J. Nucl. Mater. 35 (1970) 14.
[17] R. Guillen, F.L. Feron, J.L. Glimois, F. Hunt, J. Le Pape and J. Senevat, Textures Microstructures 14–18 (1991) 519.
[18] R. Lebensohn and G. Canova, Acta Metall. Mater., to be published.